science.sciencemag.org/cgi/content/full/science.aay3999/DC1

Supplementary Materials for

The geology and geophysics of Kuiper Belt object (486958) Arrokoth

J. R. Spencer*, S. A. Stern, J. M Moore, H. A. Weaver, K. N. Singer, C. B Olkin, A. J. Verbiscer, W. B. McKinnon, J. Wm. Parker, R. A. Beyer, J. T. Keane, T. R. Lauer, S. B. Porter, O. L. White, B. J. Buratti, M. R. El-Maarry, C. M. Lisse, A. H. Parker, H. B. Throop, S. J. Robbins, O. M. Umurhan, R. P. Binzel, D. T. Britt, M. W. Buie, A. F. Cheng, D. P. Cruikshank, H. A. Elliott, G. R. Gladstone, W. M. Grundy, M. E. Hill, M. Horanyi, D. E. Jennings, J. J. Kavelaars, I. R. Linscott, D. J. McComas, R. L. McNutt Jr., S. Protopapa, D. C. Reuter, P. M. Schenk, M. R. Showalter, L. A. Young, A. M. Zangari, A. Y. Abedin, C. B. Beddingfield, S. D. Benecchi, E. Bernardoni, C. J. Bierson, D. Borncamp, V. J. Bray, A. L. Chaikin, R. D. Dhingra, C. Fuentes, T. Fuse, P. L Gay, S. D. J. Gwyn, D. P. Hamilton, J. D. Hofgartner, M. J. Holman, A. D. Howard, C. J. A. Howett, H. Karoji, D. E. Kaufmann, M. Kinczyk, B. H. May, M. Mountain, M. Pätzold, J. M. Petit, M. R. Piquette, I. N. Reid, H. J. Reitsema, K. D. Runyon, S. S. Sheppard, J. A. Stansberry, T. Stryk, P. Tanga, D. J. Tholen, D. E. Trilling, L. H. Wasserman

*Corresponding author. Email: spencer@boulder.swri.edu

Published 13 February 2020 on *Science* First Release
DOI: 10.1126/science.aay3999

This PDF file includes:

Other Supplementary Materials for this manuscript include the following:
(available at science.sciencemag.org/cgi/content/full/science.aay3999/DC1)

Data S1 to S3

Materials and Methods

Image Processing

Each set of LORRI images of Arrokoth consists of multiple consecutive frames. In the case of the closest approach ("CA") image sets (Table S1), the images were taken during simultaneous scans by the Ralph instrument, and thus include some motion smear. For each image set, frames are registered by shifting, scaling, and rotating as necessary, and are stacked to improve the SNR. This stacking process removes features such as image defects and background stars, which are not present at the same location relative to Arrokoth in every frame. Finally, images are deconvolved to remove much of the LORRI point-spread function, and also to remove motion smear in the case of the CA image sets, to produce the final images used for analysis.

Construction of Stereo Models

Three sets of LORRI images, CA04, CA05, and CA06 (Table S1) provide the highest-resolution stereo coverage. The CA05 / CA06 pair has the best nominal resolution and a stereo convergence angle of 17°. However, the CA04 / CA06 pair (Fig. 1A) provides better stereo because, in addition to a slightly larger convergence angle (almost 20°), CA04 has a much longer effective exposure time (thus better SNR), and also lower smear, than CA05 (Table S1). We used the Ames Stereo Pipeline (*80*,*81*) on the stacked, deconvolved products from the CA04 & CA06 observations to derive a stereographic terrain model of the surface of Arrokoth. An iterative closest point algorithm (*82*,*83*) was used to rigidly rotate and translate the stereo model surface to match the -Z facing surface of the global shape model, though the required rotation was < 0.5º

Geomorphological Mapping of Arrokoth

Constructing a planetary geomorphological map derived solely from images acquired above the study area involves defining and characterizing discrete material units based primarily on the surface morphology, texture, albedo, and color as seen at the pixel scale, which are physical attributes that are related to the geologic processes that produced them. Along with visible structural features, the distributions of these units are then mapped to identify the relative roles of different geological processes that shape planetary surfaces. We have followed standard US Geological Survey mapping protocol (*84*) when creating our geomorphological map of Arrokoth (Fig. 1C), although applying the principles of mapping to it can be challenging, primarily because our highest resolution observations of the target (138 to 33 m pixel^{-1}) were only obtained at relatively low phase angles (12.9° to 32.5°). Outside a narrow strip near the terminator, the low phase angle hinders assessment of topography at a scale of hundreds of meters based on surface shading. In addition, the consistently low phase of the approach imaging generates uncertainty regarding how much of the observed surface heterogeneity across Arrokoth is due to intrinsic geological variation, or is a consequence of variable illumination of a limited range of geomorphological units. We have created a geomorphological, rather than a geological map, i.e. the units that we have defined for Arrokoth have been inferred from what appear to be distinct physiographic components of the two lobes, but the map is not intended to rigorously convey stratigraphic relations between units. Stratigraphic organization of the units would require application of the rules of superposition and crosscutting, which we do not consider to be feasible given the limitations of available data and inherent ambiguities associated with its interpretation. Instead, the map is intended to reduce the complexity of Arrokoth's surface to comprehensible proportions that are more amenable to the development of hypotheses for the formation and evolution of Arrokoth.

On the large lobe, which shows less overall albedo variation but more limb topographic amplitude than the small lobe, the boundaries of the individual sub-units that compose the lobe have been defined based largely on topographic expression in the LORRI CA06 33 m pixel^{-1} imaging, and in stereo imaging (e.g. comparing LORRI CA04 and CA06 in Fig. 1A). High solar incidence angles near the terminator make troughs and scarps separating sub-units visible in this region (including those separating units *ta, tb*, *tc*, and *sm*). In contrast, the boundary of unit *tg*, located on the limb of the large lobe, is inferred not based on shading due to topography, but due to it being ringed by bright material (unit *bm*), which we interpret to be loosely-consolidated material that has collected in depressions across Arrokoth, particularly at the neck connecting the two lobes. Stereo imaging is necessary for the identification of unit *tf* as a separate unit, as its apparent position can be seen to move relative to unit *te* between LORRI CA04 and CA06. While albedo variation across the large lobe is less than on the small lobe, some units are distinguished by their albedo characteristics, such as units *ta*, *tc*, and *td*, which appear lighter-toned than the neighboring units of *te*, *th*, and *sm*, despite these latter units being illuminated at lower solar incidence angles. Unit *tg* is distinguished from unit *te* by the partial stretch of bright material that exists between them, and because unit *tg* displays a surface pattern characterized by albedo contrasts on a scale of hundreds of meters, whereas unit *te* appears dark and homogeneous at this scale. The boundary between units *sm* and *th* is located in the center of the face of the large lobe, far from the terminator and the limb, and there is no apparent topographic discontinuity associated with it. Instead, a tentative contact has been defined based on the differing textures presented by these units (unit *th* shows greater albedo contrast than unit *sm*) as well as the presence of a portion of the bright annulus that separates them, although we have identified locations where some darker elements of unit *th*, apparently hills, extend across the annulus. We treat the distinct physiographic units on the large lobe as individual geomorphological units, although it is possible that they are in fact all topographic expressions of the same unit.

On the small lobe, units are defined primarily according to the different albedos and planforms they present; any topographic signatures associated with them are much less apparent when compared with those of sub-units under similar lighting conditions on the large lobe, which is at least in part due to the smaller scales of the small lobe's units. The small lobe's limb topography, however, does indicate a break in slope that corresponds to the stretch of dark material (unit *dm*) that separates units *mm* and *rm*, and suggests that unit *mm* occupies a local high, whereas unit *rm* occupies a local low. This topographic discontinuity is an important factor in the decision to map these areas as separate units: whereas unit *rm* displays a pitted surface and unit *mm* does not, the two units cannot be mapped separately based on this criterion alone, as we cannot rule out that variable illumination has played a role in contributing to their different appearances, given the more oblique lighting of unit *rm*.

These examples demonstrate how we considered every aspect of available imaging (in particular stereo parallax, surface shading at low and high solar incidence angles, and limb topography to identify discrete geomorphological units given the limited data available.

The R Value Measure of Crater Densities

The R value plotted on Fig. 6B is constructed from a differential power law size-frequency distribution of crater diameters ($dN/dD \propto D^q$) normalized by a D^{-3} distribution, where N is the crater spatial density and D is the diameter. The power law exponent (q) is commonly referred to as the distribution log-log slope. In this visualization, a crater size-frequency distribution

with a slope q of -3 appears as a horizontal line, allowing differences from the common D^{-3} distribution to be easily seen.

Crater Identification and Classification

Feature size measurements were carried out on the original deconvolved CA06 LORRI image (Fig 1A). As no projection was used, the crater sizes were measured in pixels and converted to approximate sizes using the pixel scale of 33 m px^{-1}. We measured the most representative diameter of a feature (e.g., measuring the long axis of obliquely viewed features to avoid foreshortening where possible). The size for the crater Maryland is an average of 6 chords. Some features have more distinct boundaries than others. For interpreting crater diameters given here, we use a diameter uncertainty, tabulated in Data S3, of 2 pixels or 20% of the crater diameter, whichever is larger for a given feature (i.e., for feature diameters above 10 pixels, or ~330 m, we use 20%).

Data S3 includes the crater sizes and subgroup designations for each feature considered for crater analysis and shown in Fig. 6A. Some features were determined to have a low likelihood of being either fresh or modified impact craters, and thus are not included in any subgroup plotted in Fig. 6B. The descriptions for each subset are:

- The A_High (Arrokoth high confidence) subgroup includes only features 0.34 km (~10 pixels) or larger in diameter, only fairly circular features, and features with the topography expected of impact craters. This subset includes a few features that are more subtle or shallow than the deepest probable craters on Arrokoth, but they are all close to the terminator where the low sun angle makes clear their likely identification as impact craters.
- The A_Medium (Arrokoth medium confidence) subgroup includes smaller and/or less circular features. It includes 4 features less than 0.34 km in diameter, from ~0.23 – 0.27 km across.
- The A_Low (Arrokoth low confidence) subgroup includes features that are depressions or bright spots but considerably less circular, and features in a chain that may be associated with a tectonic feature (at a subunit boundary). It includes 6 features less than 0.34 km in diameter, from ~0.19 – 0.28 km across.
- The LL_Bright (Large lobe bright spot) subgroup, designed to give an approximation of a maximum density, includes: all A_High, A_Medium, and A_Low features larger than 0.27 km (8 pixels), that are bright, circular or sub-circular features on the sunward half of the large lobe only (right of the solid line in Fig. 6A).
- The A_Pits (Arrokoth pits) subgroup, designed to give an approximation of a maximum density, includes all A_High, A_Medium, and A_Low features larger than 0.27 km, both circular and sub-circular, and also includes few features in a chain, that are on the anti-sunward half of the large lobe only (left of the solid line in Fig. 6A).
- The LL_Term (Large lobe terminator) subgroup, designed to give an approximation of a maximum density, includes: all A_High, A_Medium, and A_Low features larger than 0.27 km, both circular and sub-circular, and a few features that may be in a chain, in the near-terminator region left of the dashed line on Fig. 6A.

Additional information is in Table S2.

Details of Satellite Searches

Searches conducted to assess flyby hazards from 42 to 19 days before the flyby covered the entire Hill sphere (~40,000 km radius assuming an Arrokoth density of 500 kg m^{-3}) with a range of total exposure times up to 1 hour. Later 2×2 and 4×4 frame image mosaics, taken from 3.3

days to 6 hours before the flyby with 2.6 – 12 minute total exposures, covered smaller regions with greater sensitivity. Each search consisted of 2 – 3 mosaics taken 0.6 – 2.0 hours apart, to identify satellites by their motion relative to the dense Milky Way star background. These deep searches overexposed Arrokoth and thus had limited sensitivity very close to it, so close approach images exposed for Arrokoth's surface were used to search for satellites with very small orbital radii. Sensitivity limits were established by implanting synthetic objects into the original images.

Supplementary Text

Expected Impact Crater Morphologies

Despite the low impact velocities, we expect most impacts on Arrokoth to form craters similar to those seen elsewhere in the Solar System. Crater morphology varies with the impactor and target characteristics. The low and high velocity tails of the expected impact velocity distribution for Arrokoth reach down to a few m s-1 and as high as a few km s-1, but the mode, ~300 m s-1 (5), is slow compared to primary cratering velocities on the surfaces of both icy and rocky bodies closer to the Sun, and is more typical of secondary cratering velocities on those bodies (*85*, *86*). These impacts often form craters with similar morphological characteristics to primary craters, although secondary craters are often shallower than the same size primary impact, and may be elongated in the direction radial to the primary crater. We do not suggest that any craters on Arrokoth are secondary craters, but secondary craters elsewhere show that 300 m s-1 impacts are capable of creating craters on the surface of Arrokoth. The formation of a crater on a slope or modification by later geologic processes (such as mass wasting or a subsequent fault near the crater) may also alter the crater's appearance.

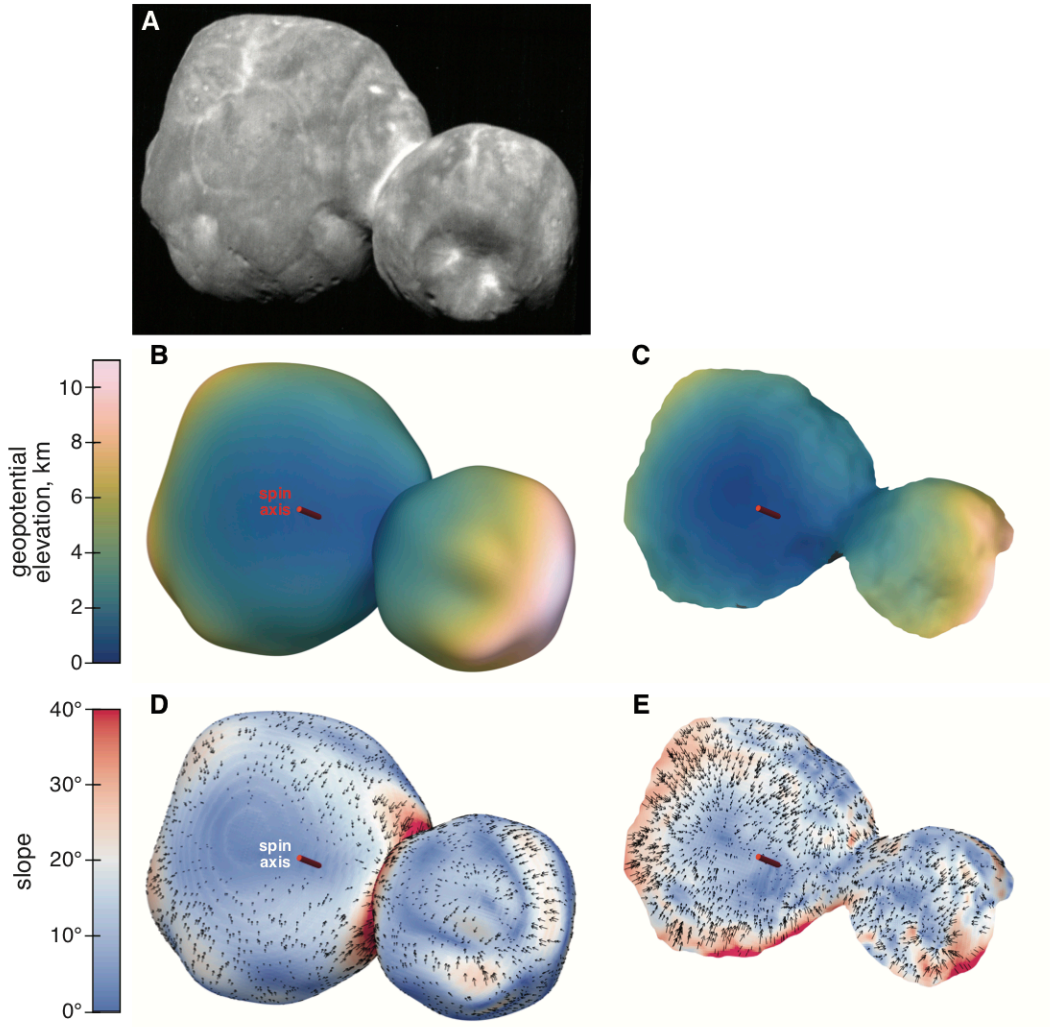

Fig. S1. Slopes and Gravity of Arrokoth. CA06 image of Arrokoth (A) compared to illustrations of gravitational parameters seen from the same geometry. B and C: Geopotential elevation for the global shape model (B) and stereo model (C). D and E: Slopes computed from the global shape model (D) and stereo model (E), for an assumed density of 500 kg m-3. Color gives slope magnitude, and arrows give the slope direction.

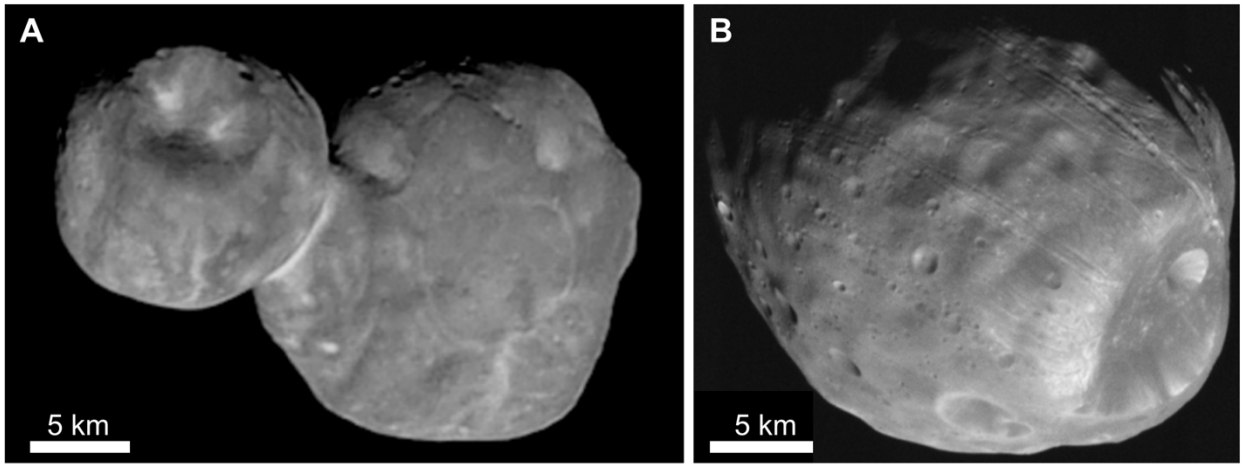

Fig. S2. Craters on Arrokoth compared to those on the Martian moon Phobos. A: Our highest resolution Arrokoth image (CA06) at 32° phase. B: An image of the Martian moon Phobos (right, diameter = 22.5 km) from the Mars Reconnaissance Orbiter, obtained at a similar but slightly lower phase angle (26.4°) (Credit: NASA/JPL-Caltech/University of Arizona). The image of Phobos has been processed to match the pixel scale, smear, camera point-spread-function, SNR, and deconvolution of our highest resolution LORRI images of Arrokoth (*87*). Many more unambiguous craters can be seen across the surface of Phobos than on Arrokoth.

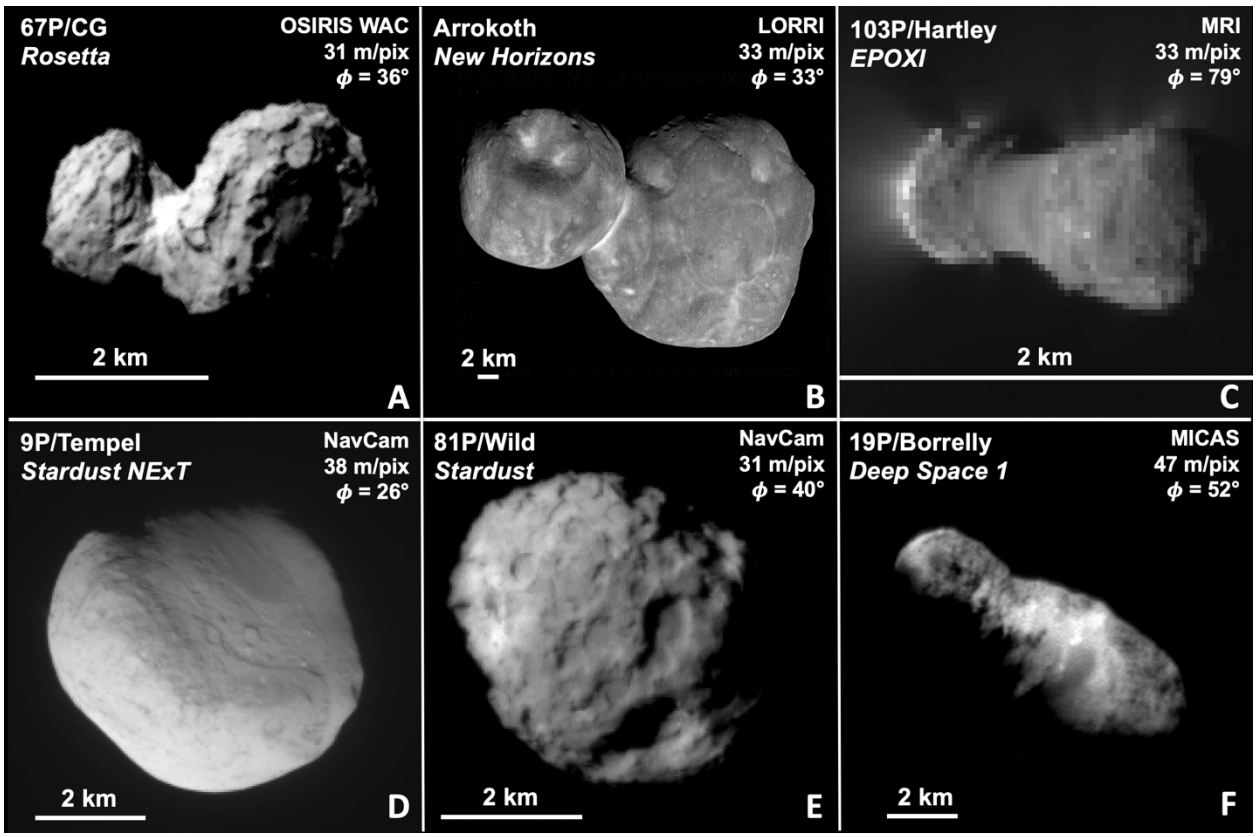

Fig. S3. Images of JFC nuclei and Arrokoth at comparable pixel scale. A: Rosetta (*73*); B: New Horizons (this paper); C: EPOXI (*74*); D and E: Stardust (*75*,*76*); F: Deep Space 1 (*77*). For higher-resolution image comparisons, and additional details, see Fig. 8.

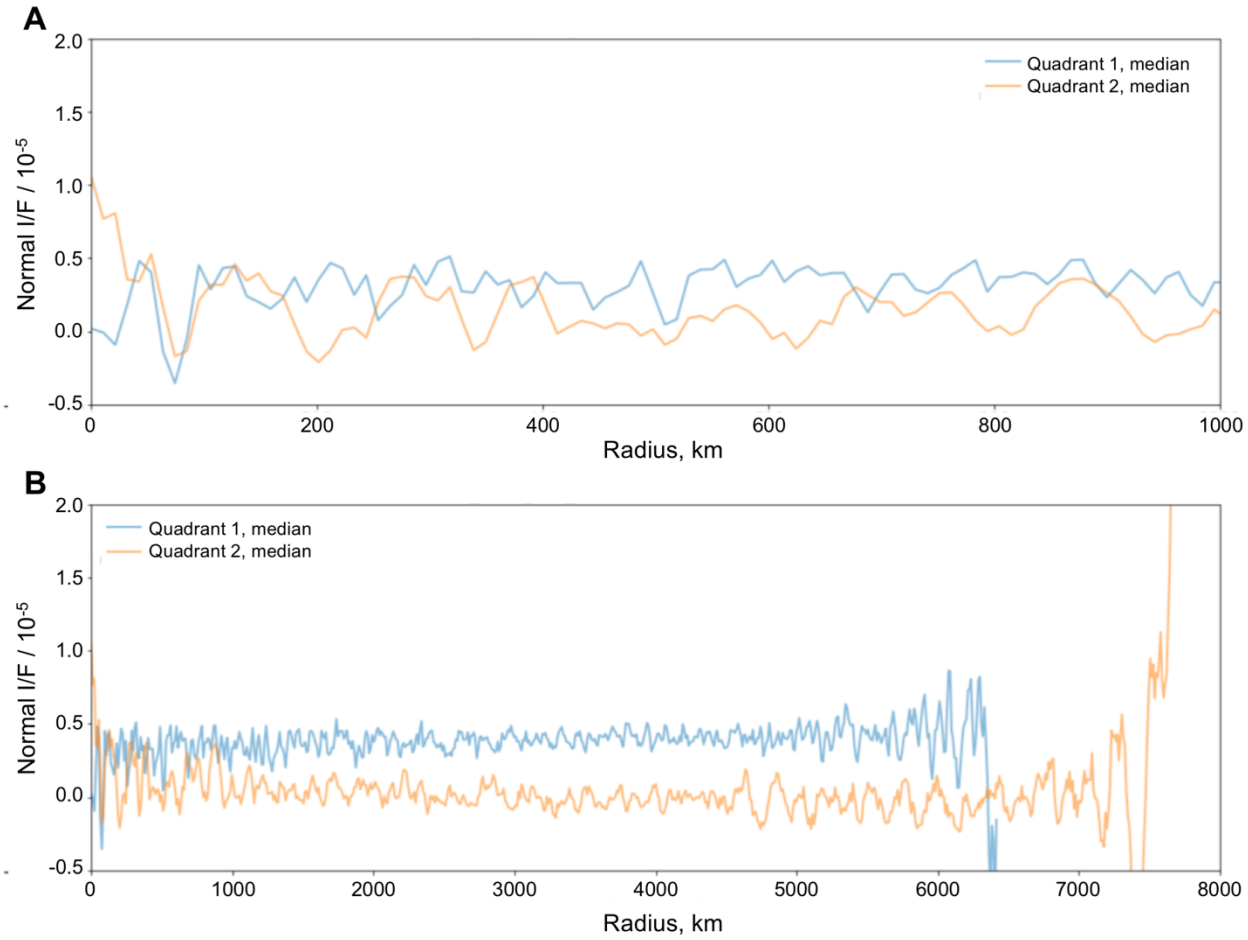

Fig. S4. Non-Detection of forward-scattering rings around Arrokoth. Radial profiles of the sky brightness, in units of I/F (*19*), as a function of distance from Arrokoth in its equatorial plane, from MVIC images taken 1.7 – 2.3 hours after closest approach at a phase-angle of 168º. A: The innermost region. B: The entire profile. The blue and orange curves were derived from different quadrants of the image: the vertical offset between them is an artifact. Profiles are binned to a radial resolution of 10.6 km. No rings or dust structures were seen, with an upper limit I/F of ~1.5×10^{-6} for structures wider than about 10 km.

Table S1. **Close approach LORRI images**. The image set name "CAnn" refers to the n^{th} observation of the close approach (C/A) sequence. CA03 and CA08, not listed here, were radiometric, not imaging, observations.

Image set name	Mode	Mid-Time, mins. after C/A	Range, km	Phase, degrees	Resolution, km pixel^{-1}	Smear, pixels	Single-Frame Exposure Time, sec	Number of Co-added Frames	Combined Exposure Time, sec
CA01	LORRI 1×1	-70.6	61,214	11.8	0.304	0.6	0.150	43	6.45
CA02	LORRI 1×1	-49.1	42,663	12.0	0.212	4.0	0.025	6	0.15
CA04	LORRI 1×1	-31.9	27,850	12.9	0.138	0.4	0.100	25	2.50
CA05	LORRI 1×1	-18.8	16,680	15.7	0.083	4.0	0.025	6	0.15
CA06	LORRI 1×1	-6.5	6,634	32.5	0.033	4.0	0.025	6	0.15
CA07	LORRI 4×4	9.4	8,834	152.4	0.175	8.1	0.200	6	1.20

Table S2. Feature subgroups for crater analysis. Data S3 includes the full list of craters and sizes with classification information. The diameter range column does not include Maryland (6.7 km diameter), which is treated separately.

Subgroup	Lobe where Present	Number of features	Diameter range (km)	Surface area used (km^2)	Area description
A_High	Both lobes	10	0.34–7.16	700	Entire visible surface of Arrokoth: Area is ½ of the global shape model surface area
A_Medium	Both lobes	17	0.24–0.64		
A_Low	Both lobes	16	0.19–0.68		
LL_Bright	Large lobe only	10	0.27–0.62	230	Sunward half of large lobe: Area is ½ of large lobe's visible surface area
LL_Pits	Large lobe only	14	0.27–0.77	230	Anti-sunward half of large lobe: Area is ½ of large lobe's visible surface area
LL_Term	Large lobe only	8	0.27–0.77	90	Measured from the shape model for the selected area

Table S3. **Properties of Arrokoth compared to cometary nuclei**. The object IDs are listed in the first column. The second column refers to the best fit ellipsoid dimensions, even though the actual shape may differ significantly from an ellipsoid. The effective spherical diameters, calculated from the best fit ellipsoidal dimensions in the second column, are presented in the third column and provide perhaps the best single number for the size of the object. The density for 67P is exceedingly well determined (*16*) and lies roughly in the middle of the ranges estimated for JFC nuclei. Due to the jetting force from cometary outgassing, the rotational periods of JFC nuclei change with time, so only approximate current values are listed for them. The JFC geometric albedos are for a wavelength of 550 nm (V-band) and are taken from (*88*,*89*), sometimes with small corrections to transform from R-band (650 nm) to V-band using the typical value for JFC colors as reported in (*90*). The geometric albedo for Arrokoth (this work) is for a wavelength of 600 nm. The variation of reflectance across the surfaces of the JFC nuclei and Arrokoth are comparable (±15-20% variation about the global mean value), except for 19P, which shows a variation about twice that of the other objects, apparently associated with two different types of terrains (*78*).

Object ID	**Ellipsoid Axes (km)**	**Spherical Diameter (km)**	**Density (kg m^{-3})**	**Rotational Period (hr)**	**Geometric Albedo**
Arrokoth	36 × 20 × 10	18.3	>290	15.9	0.23
9P/Tempel	7.6 × 4.9 × 4.6	5.6	200-600	~41	0.056
19P/Borrelly	8.0 × 3.2 × 3.2	4.3	290-830	~25	0.065
67P/Churyumov-Gerasimenko	4.3 × 2.6 × 2.1	2.9	538 ± 1	~12	0.058
81P/Wild	5.5 × 4.0 × 3.3	4.2	-	-	0.059
103P/Hartley	2.2 × 0.5 × 0.5	0.92	200-400	~18	0.045

Additional Data S1 (Separate file)

Stereo shape model of the surface of Arrokoth that was visible to New Horizons near closest approach, derived from the CA04 and CA06 LORRI images.

Additional Data S2 (Separate file)

Global shape model of Arrokoth, obtained from the complete set of LORRI images.

Data S3 (Separate file)

This table lists the identification numbers for the craters and pits shown in Fig. 6A, their diameters, diameter uncertainties, and the confidence classes and geographical groupings assigned to each.

References and Notes

1. S. A. Stern, H. A. Weaver, J. R. Spencer, C. B. Olkin, G. R. Gladstone, W. M. Grundy, J. M. Moore, D. P. Cruikshank, H. A. Elliott, W. B. McKinnon, J. W. Parker, A. J. Verbiscer, L. A. Young, D. A. Aguilar, J. M. Albers, T. Andert, J. P. Andrews, F. Bagenal, M. E. Banks, B. A. Bauer, J. A. Bauman, K. E. Bechtold, C. B. Beddingfield, N. Behrooz, K. B. Beisser, S. D. Benecchi, E. Bernardoni, R. A. Beyer, S. Bhaskaran, C. J. Bierson, R. P. Binzel, E. M. Birath, M. K. Bird, D. R. Boone, A. F. Bowman, V. J. Bray, D. T. Britt, L. E. Brown, M. R. Buckley, M. W. Buie, B. J. Buratti, L. M. Burke, S. S. Bushman, B. Carcich, A. L. Chaikin, C. L. Chavez, A. F. Cheng, E. J. Colwell, S. J. Conard, M. P. Conner, C. A. Conrad, J. C. Cook, S. B. Cooper, O. S. Custodio, C. M. Dalle Ore, C. C. Deboy, P. Dharmavaram, R. D. Dhingra, G. F. Dunn, A. M. Earle, A. F. Egan, J. Eisig, M. R. El-Maarry, C. Engelbrecht, B. L. Enke, C. J. Ercol, E. D. Fattig, C. L. Ferrell, T. J. Finley, J. Firer, J. Fischetti, W. M. Folkner, M. N. Fosbury, G. H. Fountain, J. M. Freeze, L. Gabasova, L. S. Glaze, J. L. Green, G. A. Griffith, Y. Guo, M. Hahn, D. W. Hals, D. P. Hamilton, S. A. Hamilton, J. J. Hanley, A. Harch, K. A. Harmon, H. M. Hart, J. Hayes, C. B. Hersman, M. E. Hill, T. A. Hill, J. D. Hofgartner, M. E. Holdridge, M. Horányi, A. Hosadurga, A. D. Howard, C. J. A. Howett, S. E. Jaskulek, D. E. Jennings, J. R. Jensen, M. R. Jones, H. K. Kang, D. J. Katz, D. E. Kaufmann, J. J. Kavelaars, J. T. Keane, G. P. Keleher, M. Kinczyk, M. C. Kochte, P. Kollmann, S. M. Krimigis, G. L. Kruizinga, D. Y. Kusnierkiewicz, M. S. Lahr, T. R. Lauer, G. B. Lawrence, J. E. Lee, E. J. Lessac-Chenen, I. R. Linscott, C. M. Lisse, A. W. Lunsford, D. M. Mages, V. A. Mallder, N. P. Martin, B. H. May, D. J. McComas, R. L. McNutt Jr., D. S. Mehoke, T. S. Mehoke, D. S. Nelson, H. D. Nguyen, J. I. Núñez, A. C. Ocampo, W. M. Owen, G. K. Oxton, A. H. Parker, M. Pätzold, J. Y. Pelgrift, F. J. Pelletier, J. P. Pineau, M. R. Piquette, S. B. Porter, S. Protopapa, E. Quirico, J. A. Redfern, A. L. Regiec, H. J. Reitsema, D. C. Reuter, D. C. Richardson, J. E. Riedel, M. A. Ritterbush, S. J. Robbins, D. J. Rodgers, G. D. Rogers, D. M. Rose, P. E. Rosendall, K. D. Runyon, M. G. Ryschkewitsch, M. M. Saina, M. J. Salinas, P. M. Schenk, J. R. Scherrer, W. R. Schlei, B. Schmitt, D. J. Schultz, D. C. Schurr, F. Scipioni, R. L. Sepan, R. G. Shelton, M. R. Showalter, M. Simon, K. N. Singer, E. W. Stahlheber, D. R. Stanbridge, J. A. Stansberry, A. J. Steffl, D. F. Strobel, M. M. Stothoff, T. Stryk, J. R. Stuart, M. E. Summers, M. B. Tapley, A. Taylor, H. W. Taylor, R. M. Tedford, H. B. Throop, L. S. Turner, O. M. Umurhan, J. Van Eck, D. Velez, M. H. Versteeg, M. A. Vincent, R. W. Webbert, S. E. Weidner, G. E. Weigle 2nd, J. R. Wendel, O. L. White, K. E. Whittenburg, B. G. Williams, K. E. Williams, S. P. Williams, H. L. Winters, A. M. Zangari, T. H. Zurbuchen, Initial results from the New Horizons exploration of 2014 MU_{69}, a small Kuiper Belt object. *Science* **364**, eaaw9771 (2019). doi:10.1126/science.aaw9771 Medline

2. S. B. Porter, M. W. Buie, A. H. Parker, J. R. Spencer, S. Benecchi, P. Tanga, A. Verbiscer, J. J. Kavelaars, S. D. J. Gwyn, E. F. Young, H. A. Weaver, C. B. Olkin, J. W. Parker, S. A. Stern, High-precision orbit fitting and uncertainty analysis of (486958) 2014 MU69. *Astron. J.* **156**, 20 (2018). doi:10.3847/1538-3881/aac2e1

3. W. M. Grundy *et al*., Color, composition, and thermal environment of Kuiper Belt object (486958) Arrokoth. *Science* 10.1126/science.aay3705 (2020).

4. J.-M. Petit, J. J. Kavelaars, B. J. Gladman, R. L. Jones, J. W. Parker, C. Van Laerhoven, P. Nicholson, G. Mars, P. Rousselot, O. Mousis, B. Marsden, A. Bieryla, M. Taylor, M. L. N. Ashby, P. Benavidez, A. Campo Bagatin, G. Bernabeu, The Canada-France Ecliptic Plane Survey - full data release: The orbital structure of the Kuiper belt. *Astron. J.* **142**, 131 (2011). doi:10.1088/0004-6256/142/4/131

5. S. Greenstreet, B. Gladman, W. B. McKinnon, J. J. Kavelaars, K. N. Singer, Crater density Predictions for New Horizons flyby target 2014 MU69. *Astrophys. J.* **872**, L5 (2019). doi:10.3847/2041-8213/ab01db

6. S. Greenstreet, B. Gladman, W. B. McKinnon, Impact and cratering rates onto Pluto. *Icarus* **258**, 267–288 (2015). doi:10.1016/j.icarus.2015.05.026

7. A. F. Cheng, H. A. Weaver, S. J. Conard, M. F. Morgan, O. Barnouin-Jha, J. D. Boldt, K. A. Cooper, E. H. Darlington, M. P. Grey, J. R. Hayes, K. E. Kosakowski, T. Magee, E. Rossano, D. Sampath, C. Schlemm, H. W. Taylor, Long-Range Reconnaissance Imager on New Horizons. *Space Sci. Rev.* **140**, 189–215 (2008). doi:10.1007/s11214-007-9271-6

8. D. C. Reuter, S. A. Stern, J. Scherrer, D. E. Jennings, J. W. Baer, J. Hanley, L. Hardaway, A. Lunsford, S. McMuldroch, J. Moore, C. Olkin, R. Parizek, H. Reitsma, D. Sabatke, J. Spencer, J. Stone, H. Throop, J. Van Cleve, G. E. Weigle, L. A. Young, Ralph: A Visible/Infrared Imager for the New Horizons Pluto/Kuiper Belt mission. *Space Sci. Rev.* **140**, 129–154 (2008). doi:10.1007/s11214-008-9375-7

9. Materials and methods are available as supplementary materials.

10. S. D. Benecchi, S. B. Porter, M. W. Buie, A. M. Zangari, A. J. Verbiscer, K. S. Noll, S. A. Stern, J. R. Spencer, A. H. Parker, The HST lightcurve of (486958) 2014 MU69. *Icarus* **334**, 11–21 (2019). doi:10.1016/j.icarus.2019.01.023

11. M. W. Buie *et al*., Size and shape constraints of (486958) Arrokoth from stellar occultations (2020). https://arxiv.org/abs/2001.00125.

12. A. M. Zangari, *et al.*, The mysterious missing light curve of (486958) 2014 MU69, a bi-lobate contact binary visited by New Horizons. *Lunar Planet. Sci. Conf.* 3007 (2019).

13. A. Thirouin, S. S. Sheppard, Light curves and rotational properties of the pristine Cold Classical Kuiper Belt objects. *Astron. J.* **157**, 228 (2019). doi:10.3847/1538-3881/ab18a9

14. S. B. Porter *et al*., New Horizons distant observations of Cold Classical KBOs. AAS/Division for Planetary Sciences Meeting Abstracts 509.07 (2018).

15. A. J. Verbiscer, S. Porter, S. D. Benecchi, J. J. Kavelaars, H. A. Weaver, J. R. Spencer, M. W. Buie, D. Tholen, B. J. Buratti, P. Helfenstein, A. H. Parker, C. B. Olkin, J. Parker, S. A. Stern, L. A. Young, K. Ennico-Smith, K. N. Singer, A. F. Cheng, C. M. Lisse, Phase curves from the Kuiper belt: Photometric properties of "distant" KBOs observed by New Horizons. *Astron. J.* **158**, 123 (2019). doi:10.3847/1538-3881/ab3211

16. F. Preusker, F. Scholten, K.-D. Matz, T. Roatsch, S. F. Hviid, S. Mottola, J. Knollenberg, E. Kührt, M. Pajola, N. Oklay, J.-B. Vincent, B. Davidsson, M. F. A'Hearn, J. Agarwal, C. Barbieri, M. A. Barucci, J.-L. Bertaux, I. Bertini, G. Cremonese, V. Da Deppo, S. Debei, M. De Cecco, S. Fornasier, M. Fulle, O. Groussin, P. J. Gutiérrez, C. Güttler, W.-H. Ip, L. Jorda, H. U. Keller, D. Koschny, J. R. Kramm, M. Küppers, P. Lamy, L. M. Lara, M.

Lazzarin, J. J. Lopez Moreno, F. Marzari, M. Massironi, G. Naletto, H. Rickman, R. Rodrigo, H. Sierks, N. Thomas, C. Tubiana, The global meter-level shape model of comet 67P/Churyumov-Gerasimenko. *Astron. Astrophys.* **607**, L1 (2017). doi:10.1051/0004-6361/201731798

17. D. J. Scheeres, *Orbital Motion in Strongly Perturbed Environments: Applications to Asteroids, Comet and Planetary Satellite Orbiters* (Springer-Praxis, Chichester, 2012).

18. W. B. McKinnon *et al*., The solar nebula origin of (486958) Arrokoth, a primordial contact binary in the Kuiper Belt. *Science* 10.1126/science.aay6620 (2020).

19. Normal reflectance is the I/F (where I is the scattered intensity from the surface and πF is the solar flux at the distance of the scattering surface; also called the bidirectional reflectance) when the incident and emission angles are both zero.

20. B. Buratti, J. Veverka, J., Voyager photometry of Europa. *Icarus* **55**, 93–110 (1983). doi:10.1016/0019-1035(83)90053-2

21. S. Besse, P. Lamy, L. Jorda, S. Marchi, C. Barbieri, Identification and physical properties of craters on Asteroid (2867) Steins. *Icarus* **221**, 1119–1129 (2012). doi:10.1016/j.icarus.2012.08.008

22. M. S. Robinson, P. C. Thomas, J. Veverka, S. L. Murchie, B. B. Wilcox, The geology of 433 Eros. *Meteorit. Planet. Sci.* **37**, 1651–1684 (2002). doi:10.1111/j.1945-5100.2002.tb01157.x

23. L. Prockter, P. Thomas, M. Robinson, J. Joseph, A. Milne, B. Bussey, J. Veverka, A. Cheng, Surface expressions of structural features on Eros. *Icarus* **155**, 75–93 (2002). doi:10.1006/icar.2001.6770

24. D. L. Buczkowski, O. S. Barnouin-Jha, L. M. Prockter, 433 Eros lineaments: Global mapping and analysis. *Icarus* **193**, 39–52 (2008). doi:10.1016/j.icarus.2007.06.028

25. S. J. Morrison, P. C. Thomas, M. S. Tiscareno, J. A. Burns, J. Veverka, Grooves on small Saturnian satellites and other objects: Characteristics and significance. *Icarus* **204**, 262–270 (2009). doi:10.1016/j.icarus.2009.06.003

26. T. A. Hurford, E. Asphaug, J. N. Spitale, D. Hemingway, A. R. Rhoden, W. G. Henning, B. G. Bills, S. A. Kattenhorn, M. Walker, Tidal disruption of Phobos as the cause of surface fractures. *J. Geophys. Res. Planets* **121**, 1054–1065 (2016). doi:10.1002/2015JE004943

27. S. A. Stern, The evolution of comets in the Oort cloud and Kuiper belt. *Nature* **424**, 639–642 (2003). doi:10.1038/nature01725 Medline

28. M. J. S. Belton, P. Thomas, J. Veverka, P. Schultz, M. F. A'Hearn, L. Feaga, T. Farnham, O. Groussin, J.-Y. Li, C. Lisse, L. McFadden, J. Sunshine, K. J. Meech, W. A. Delamere, J. Kissel, The internal structure of Jupiter family cometary nuclei from Deep Impact observations: The "talps" or "layered pile" model. *Icarus* **187**, 332–344 (2007). doi:10.1016/j.icarus.2006.09.005

29. M. Jutzi, E. Asphaug, The shape and structure of cometary nuclei as a result of low-velocity accretion. *Science* **348**, 1355–1358 (2015). 10.1126/science.aaa4747 Medline

30. K. R. Housen, W. J. Sweet, K. A. Holsapple, Impacts into porous asteroids. *Icarus* **300**, 72–96 (2018). doi:10.1016/j.icarus.2017.08.019

31. S. J. Robbins, W. A. Watters, J. E. Chappelow, V. J. Bray, I. J. Daubar, R. A. Craddock, R. A. Beyer, M. Landis, L. R. Ostrach, L. Tornabene, J. D. Riggs, B. P. Weaver, Measuring impact crater depth throughout the solar system. *Meteorit. Planet. Sci.* **53**, 583–637 (2018). doi:10.1111/maps.12956

32. K. A. Holsapple, K. R. Housen, A crater and its ejecta: An interpretation of Deep Impact. *Icarus* **191**, 586–597 (2007). doi:10.1016/j.icarus.2006.08.035

33. D. Nesvorný, Dynamical evolution of the early Solar System. *Annu. Rev. Astron. Astrophys.* **56**, 137–174 (2018). doi:10.1146/annurev-astro-081817-052028

34. S. Sugita, R. Honda, T. Morota, S. Kameda, H. Sawada, E. Tatsumi, M. Yamada, C. Honda, Y. Yokota, T. Kouyama, N. Sakatani, K. Ogawa, H. Suzuki, T. Okada, N. Namiki, S. Tanaka, Y. Iijima, K. Yoshioka, M. Hayakawa, Y. Cho, M. Matsuoka, N. Hirata, N. Hirata, H. Miyamoto, D. Domingue, M. Hirabayashi, T. Nakamura, T. Hiroi, T. Michikami, P. Michel, R.-L. Ballouz, O. S. Barnouin, C. M. Ernst, S. E. Schröder, H. Kikuchi, R. Hemmi, G. Komatsu, T. Fukuhara, M. Taguchi, T. Arai, H. Senshu, H. Demura, Y. Ogawa, Y. Shimaki, T. Sekiguchi, T. G. Müller, A. Hagermann, T. Mizuno, H. Noda, K. Matsumoto, R. Yamada, Y. Ishihara, H. Ikeda, H. Araki, K. Yamamoto, S. Abe, F. Yoshida, A. Higuchi, S. Sasaki, S. Oshigami, S. Tsuruta, K. Asari, S. Tazawa, M. Shizugami, J. Kimura, T. Otsubo, H. Yabuta, S. Hasegawa, M. Ishiguro, S. Tachibana, E. Palmer, R. Gaskell, L. Le Corre, R. Jaumann, K. Otto, N. Schmitz, P. A. Abell, M. A. Barucci, M. E. Zolensky, F. Vilas, F. Thuillet, C. Sugimoto, N. Takaki, Y. Suzuki, H. Kamiyoshihara, M. Okada, K. Nagata, M. Fujimoto, M. Yoshikawa, Y. Yamamoto, K. Shirai, R. Noguchi, N. Ogawa, F. Terui, S. Kikuchi, T. Yamaguchi, Y. Oki, Y. Takao, H. Takeuchi, G. Ono, Y. Mimasu, K. Yoshikawa, T. Takahashi, Y. Takei, A. Fujii, C. Hirose, S. Nakazawa, S. Hosoda, O. Mori, T. Shimada, S. Soldini, T. Iwata, M. Abe, H. Yano, R. Tsukizaki, M. Ozaki, K. Nishiyama, T. Saiki, S. Watanabe, Y. Tsuda, The geomorphology, color, and thermal properties of Ryugu: Implications for parent-body processes. *Science* **364**, eaaw0422 (2019). doi:10.1126/science.aaw0422 Medline

35. K. J. Walsh *et al*., Craters, boulders and regolith of (101955) Bennu. *Nat. Geosci.* **12**, 242–246 (2019). doi:10.1038/s41561-019-0326-6

36. D. J. Scheeres, J. W. McMahon, A. S. French, D. N. Brack, S. R. Chesley, D. Farnocchia, Y. Takahashi, J. M. Leonard, J. Geeraert, B. Page, P. Antreasian, K. Getzandanner, D. Rowlands, E. M. Mazarico, J. Small, D. E. Highsmith, M. Moreau, J. P. Emery, B. Rozitis, M. Hirabayashi, P. Sánchez, S. Van wal, P. Tricarico, R.-L. Ballouz, C. L. Johnson, M. M. Al Asad, H. C. M. Susorney, O. S. Barnouin, M. G. Daly, J. A. Seabrook, R. W. Gaskell, E. E. Palmer, J. R. Weirich, K. J. Walsh, E. R. Jawin, E. B. Bierhaus, P. Michel, W. F. Bottke, M. C. Nolan, H. C. Connolly Jr., D. S. Lauretta, The dynamic geophysical environment of (101955) Bennu based on OSIRIS-REx measurements. *Nat. Astron.* **3**, 352–361 (2019). doi:10.1038/s41550-019-0721-3

37. A. H. Parker, The intrinsic Neptune Trojan orbit distribution: Implications for the primordial disk and planet migration. *Icarus* **247**, 112–125 (2015). doi:10.1016/j.icarus.2014.09.043

38. S. Mazrouei, R. R. Ghent, W. F. Bottke, A. H. Parker, T. M. Gernon, Earth and Moon impact flux increased at the end of the Paleozoic. *Science* **363**, 253–257 (2019). doi:10.1126/science.aar4058 Medline

39. K. N. Singer, W. B. McKinnon, B. Gladman, S. Greenstreet, E. B. Bierhaus, S. A. Stern, A. H. Parker, S. J. Robbins, P. M. Schenk, W. M. Grundy, V. J. Bray, R. A. Beyer, R. P. Binzel, H. A. Weaver, L. A. Young, J. R. Spencer, J. J. Kavelaars, J. M. Moore, A. M. Zangari, C. B. Olkin, T. R. Lauer, C. M. Lisse, K. Ennico; New Horizons Geology, Geophysics and Imaging Science Theme Team; New Horizons Surface Composition Science Theme Team; New Horizons Ralph and LORRI Teams, Impact craters on Pluto and Charon indicate a deficit of small Kuiper belt objects. *Science* **363**, 955–959 (2019). doi:10.1126/science.aap8628 Medline

40. K. S. Noll, W. M. Grundy, D. Nesvorný, A. Thirouin, "Transneptunian binaries" in *The Trans-Neptunian Solar System*, D. Prialnik, M. A. Barucci, L. Young, Eds. (Elsevier, 2019), pp. 205-224.

41. W. R. Johnston, Binary Minor Planets Compilation V3.0. urn:nasa:pds:ast_binary_parameters_compilation:3.0. NASA Planetary Data System, (2019), https://sbn.psi.edu/pds/resource/binmp.html.

42. F. Marchis, J. Durech, J. Castillo-Rogez, F. Vachier, M. Cuk, J. Berthier, M. H. Wong, P. Kalas, G. Duchene, M. A. van Dam, H. Hamanowa, M. Viikinkoski, The Puzzling mutual orbit of the binary Trojan asteroid (624) Hektor. *Astrophys. J.* **783**, L37 (2014). doi:10.1088/2041-8205/783/2/L37

43. P. Descamps, F. Marchis, J. Berthier, J. P. Emery, G. Duchêne, I. de Pater, M. H. Wong, L. Lim, H. B. Hammel, F. Vachier, P. Wiggins, J.-P. Teng-Chuen-Yu, A. Peyrot, J. Pollock, M. Assafin, R. Vieira-Martins, J. I. B. Camargo, F. Braga-Ribas, B. Macomber, Triplicity and physical characteristics of Asteroid (216) Kleopatra. *Icarus* **211**, 1022–1033 (2011). doi:10.1016/j.icarus.2010.11.016

44. F. Braga-Ribas, B. Sicardy, J. L. Ortiz, C. Snodgrass, F. Roques, R. Vieira-Martins, J. I. B. Camargo, M. Assafin, R. Duffard, E. Jehin, J. Pollock, R. Leiva, M. Emilio, D. I. Machado, C. Colazo, E. Lellouch, J. Skottfelt, M. Gillon, N. Ligier, L. Maquet, G. Benedetti-Rossi, A. Ramos Gomes Jr., P. Kervella, H. Monteiro, R. Sfair, M. El Moutamid, G. Tancredi, J. Spagnotto, A. Maury, N. Morales, R. Gil-Hutton, S. Roland, A. Ceretta, S. H. Gu, X. B. Wang, K. Harpsøe, M. Rabus, J. Manfroid, C. Opitom, L. Vanzi, L. Mehret, L. Lorenzini, E. M. Schneiter, R. Melia, J. Lecacheux, F. Colas, F. Vachier, T. Widemann, L. Almenares, R. G. Sandness, F. Char, V. Perez, P. Lemos, N. Martinez, U. G. Jørgensen, M. Dominik, F. Roig, D. E. Reichart, A. P. LaCluyze, J. B. Haislip, K. M. Ivarsen, J. P. Moore, N. R. Frank, D. G. Lambas, A ring system detected around the Centaur (10199) Chariklo. *Nature* **508**, 72–75 (2014). doi:10.1038/nature13155 Medline

45. J. L. Ortiz, P. Santos-Sanz, B. Sicardy, G. Benedetti-Rossi, D. Bérard, N. Morales, R. Duffard, F. Braga-Ribas, U. Hopp, C. Ries, V. Nascimbeni, F. Marzari, V. Granata, A. Pál, C. Kiss, T. Pribulla, R. Komžík, K. Hornoch, P. Pravec, P. Bacci, M. Maestripieri, L. Nerli, L. Mazzei, M. Bachini, F. Martinelli, G. Succi, F. Ciabattari, H. Mikuz, A. Carbognani, B. Gaehrken, S. Mottola, S. Hellmich, F. L. Rommel, E. Fernández-

Valenzuela, A. C. Bagatin, S. Cikota, A. Cikota, J. Lecacheux, R. Vieira-Martins, J. I. B. Camargo, M. Assafin, F. Colas, R. Behrend, J. Desmars, E. Meza, A. Alvarez-Candal, W. Beisker, A. R. Gomes-Junior, B. E. Morgado, F. Roques, F. Vachier, J. Berthier, T. G. Mueller, J. M. Madiedo, O. Unsalan, E. Sonbas, N. Karaman, O. Erece, D. T. Koseoglu, T. Ozisik, S. Kalkan, Y. Guney, M. S. Niaei, O. Satir, C. Yesilyaprak, C. Puskullu, A. Kabas, O. Demircan, J. Alikakos, V. Charmandaris, G. Leto, J. Ohlert, J. M. Christille, R. Szakáts, A. T. Farkas, E. Varga-Verebélyi, G. Marton, A. Marciniak, P. Bartczak, T. Santana-Ros, M. Butkiewicz-Bąk, G. Dudziński, V. Alí-Lagoa, K. Gazeas, L. Tzouganatos, N. Paschalis, V. Tsamis, A. Sánchez-Lavega, S. Pérez-Hoyos, R. Hueso, J. C. Guirado, V. Peris, R. Iglesias-Marzoa, The size, shape, density and ring of the dwarf planet Haumea from a stellar occultation. *Nature* **550**, 219–223 (2017). doi:10.1038/nature24051 Medline

46. J. L. Ortiz, R. Duffard, N. Pinilla-Alonso, A. Alvarez-Candal, P. Santos-Sanz, N. Morales, E. Fernández-Valenzuela, J. Licandro, A. Campo Bagatin, A. Thirouin, Possible ring material around centaur (2060) Chiron. *Astron. Astrophys.* **576**, A18 (2015). doi:10.1051/0004-6361/201424461

47. H. B. Throop *et al*., The Jovian rings: New results derived from Cassini, Galileo, Voyager, and Earth-based observations. *Icarus* **172**, 59–77 (2004). doi:10.1016/j.icarus.2003.12.020

48. T. R. Lauer, H. B. Throop, M. R. Showalter, H. A. Weaver, S. A. Stern, J. R. Spencer, M. W. Buie, D. P. Hamilton, S. B. Porter, A. J. Verbiscer, L. A. Young, C. B. Olkin, K. Ennico, N. H. S. Team, The New Horizons and Hubble Space Telescope search for rings, dust, and debris in the Pluto-Charon system. *Icarus* **301**, 155–172 (2018). doi:10.1016/j.icarus.2017.09.033

49. M. Horányi, V. Hoxie, D. James, A. Poppe, C. Bryant, B. Grogan, B. Lamprecht, J. Mack, F. Bagenal, S. Batiste, N. Bunch, T. Chanthawanich, F. Christensen, M. Colgan, T. Dunn, G. Drake, A. Fernandez, T. Finley, G. Holland, A. Jenkins, C. Krauss, E. Krauss, O. Krauss, M. Lankton, C. Mitchell, M. Neeland, T. Reese, K. Rash, G. Tate, C. Vaudrin, J. Westfall, The Student Dust Counter on the New Horizons Mission. *Space Sci. Rev.* **140**, 387–402 (2008). doi:10.1007/s11214-007-9250-y

50. P. Lacerda, S. Fornasier, E. Lellouch, C. Kiss, E. Vilenius, P. Santos-Sanz, M. Rengel, T. Müller, J. Stansberry, R. Duffard, A. Delsanti, A. Guilbert-Lepoutre, The albedo-color diversity of transneptunian objects. *Astrophys. J.* **793**, L2 (2014). doi:10.1088/2041-8205/793/1/L2

51. A. Thirouin, S. S. Sheppard, The Plutino population: An abundance of contact binaries. *Astron. J.* **155**, 248 (2018). doi:10.3847/1538-3881/aac0ff

52. P. Thomas, J. Veverka, P. Helfenstein, Voyager observations of Nereid. *J. Geophys. Res.* **96** (S01), 19253 (1991). doi:10.1029/91JA01735

53. T. V. Johnson, J. I. Lunine, Saturn's moon Phoebe as a captured body from the outer Solar System. *Nature* **435**, 69–71 (2005). doi:10.1038/nature03384 Medline

54. W. K. Hartmann, A satellite-asteroid mystery and a possible early flux of scattered C-class asteroids. *Icarus* **71**, 57–68 (1987). doi:10.1016/0019-1035(87)90162-X

55. J. Castillo-Rogez, P. Vernazza, K. Walsh, Geophysical evidence that Saturn's Moon Phoebe originated from a C-type asteroid reservoir. *Mon. Not. R. Astron. Soc.* **486**, 538–543 (2019). doi:10.1093/mnras/stz786

56. D. P. Simonelli, J. Kay, D. Adinolfi, J. Veverka, P. C. Thomas, P. Helfenstein, Phoebe: Albedo map and photometric properties. *Icarus* **138**, 249–258 (1999). doi:10.1006/icar.1999.6077

57. B. J. Buratti, M. D. Hicks, K. A. Tryka, M. S. Sittig, R. L. Newburn, High-resolution 0.33–0.92 mm spectra of Iapetus, Hyperion, Phoebe, Rhea, Dione, and D-type asteroids: How are they related? *Icarus* **155**, 375–381 (2002). doi:10.1006/icar.2001.6730

58. C. C. Porco, E. Baker, J. Barbara, K. Beurle, A. Brahic, J. A. Burns, S. Charnoz, N. Cooper, D. D. Dawson, A. D. Del Genio, T. Denk, L. Dones, U. Dyudina, M. W. Evans, B. Giese, K. Grazier, P. Helfenstein, A. P. Ingersoll, R. A. Jacobson, T. V. Johnson, A. McEwen, C. D. Murray, G. Neukum, W. M. Owen, J. Perry, T. Roatsch, J. Spitale, S. Squyres, P. C. Thomas, M. Tiscareno, E. Turtle, A. R. Vasavada, J. Veverka, R. Wagner, R. West, Cassini Imaging Science: Initial results on Phoebe and Iapetus. *Science* **307**, 1237–1242 (2005). doi:10.1126/science.1107981 Medline

59. M. Duncan, H. Levison, L. Dones, "Dynamical evolution of ecliptic comets". In *Comets II*, M. C. Festou, H. U. Keller, H. A. Weaver Eds. (University of Arizona Press, Tucson, 193, 2004).

60. D. E. Vavilov, S. Eggl, Y. D. Medvedev, P. B. Zatitskiy, Shape evolution of cometary nuclei via anisotropic mass loss. *Astron. Astrophys.* **622**, L5 (2019). doi:10.1051/0004-6361/201834806

61. O. Groussin, N. Attree, Y. Brouet, V. Ciarletti, B. Davidsson, G. Filacchione, H.-H. Fischer, B. Gundlach, M. Knapmeyer, J. Knollenberg, R. Kokotanekova, E. Kührt, C. Leyrat, D. Marshall, I. Pelivan, Y. Skorov, C. Snodgrass, T. Spohn, F. Tosi, The thermal, mechanical, structural, and dielectric properties of cometary nuclei After Rosetta. *Space Sci. Rev.* **215**, 29 (2019). doi:10.1007/s11214-019-0594-x

62. R. Kokotanekova, C. Snodgrass, P. Lacerda, S. F. Green, S. C. Lowry, Y. R. Fernández, C. Tubiana, A. Fitzsimmons, H. H. Hsieh, Rotation of cometary nuclei: New light curves and an update of the ensemble properties of Jupiter-family comets. *Mon. Not. R. Astron. Soc.* **471**, 2974–3007 (2017). doi:10.1093/mnras/stx1716

63. D. Bodewits, T. L. Farnham, M. S. P. Kelley, M. M. Knight, A rapid decrease in the rotation rate of comet 41P/Tuttle-Giacobini-Kresák. *Nature* **553**, 186–188 (2018). doi:10.1038/nature25150 Medline

64. J. Sunshine, N. Thomas, M. R. El-Maarry, T. L. Farnham, Evidence for geologic processes on comets. *J. Geophys. Res. Planets* **121**, 2194–2210 (2016). doi:10.1002/2016JE005119

65. M. R. El-Maarry, O. Groussin, N. Thomas, M. Pajola, A.-T. Auger, B. Davidsson, X. Hu, S. F. Hviid, J. Knollenberg, C. Güttler, C. Tubiana, S. Fornasier, C. Feller, P. Hasselmann, J.-B. Vincent, H. Sierks, C. Barbieri, P. Lamy, R. Rodrigo, D. Koschny, H. U. Keller, H. Rickman, M. F. A'Hearn, M. A. Barucci, J.-L. Bertaux, I. Bertini, S. Besse, D. Bodewits, G. Cremonese, V. Da Deppo, S. Debei, M. De Cecco, J. Deller, J. D. P. Deshapriya, M. Fulle, P. J. Gutierrez, M. Hofmann, W.-H. Ip, L. Jorda, G. Kovacs, J.-R. Kramm, E.

Kührt, M. Küppers, L. M. Lara, M. Lazzarin, Z.-Y. Lin, J. J. Lopez Moreno, S. Marchi, F. Marzari, S. Mottola, G. Naletto, N. Oklay, A. Pommerol, F. Preusker, F. Scholten, X. Shi, Surface changes on comet 67P/Churyumov-Gerasimenko suggest a more active past. *Science* **355**, 1392–1395 (2017). doi:10.1126/science.aak9384 Medline

66. P. C. Thomas, M. F. A'Hearn, J. Veverka, M. J. S. Belton, J. Kissel, K. P. Klaasen, L. A. McFadden, H. J. Melosh, P. H. Schultz, S. Besse, B. T. Carcich, T. L. Farnham, O. Groussin, B. Hermalyn, J.-Y. Li, D. J. Lindler, C. M. Lisse, K. Meech, J. E. Richardson, Shape, density, and geology of the nucleus of Comet 103P/Hartley 2. *Icarus* **222**, 550–558 (2013). doi:10.1016/j.icarus.2012.05.034

67. D. T. Britt, D. C. Boice, B. J. Buratti, H. Campins, R. M. Nelson, J. Oberst, B. R. Sandel, S. A. Stern, L. A. Soderblom, N. Thomas, The morphology and surface processes of Comet 19/P Borrelly. *Icarus* **167**, 45–53 (2004). doi:10.1016/j.icarus.2003.09.004

68. N. Thomas, B. Davidsson, M. R. El-Maarry, S. Fornasier, L. Giacomini, A. G. Gracia-Berná, S. F. Hviid, W.-H. Ip, L. Jorda, H. U. Keller, J. Knollenberg, E. Kührt, F. La Forgia, I. L. Lai, Y. Liao, R. Marschall, M. Massironi, S. Mottola, M. Pajola, O. Poch, A. Pommerol, F. Preusker, F. Scholten, C. C. Su, J. S. Wu, J.-B. Vincent, H. Sierks, C. Barbieri, P. L. Lamy, R. Rodrigo, D. Koschny, H. Rickman, M. F. A'Hearn, M. A. Barucci, J.-L. Bertaux, I. Bertini, G. Cremonese, V. Da Deppo, S. Debei, M. de Cecco, M. Fulle, O. Groussin, P. J. Gutierrez, J.-R. Kramm, M. Küppers, L. M. Lara, M. Lazzarin, J. J. Lopez Moreno, F. Marzari, H. Michalik, G. Naletto, J. Agarwal, C. Güttler, N. Oklay, C. Tubiana, Redistribution of particles across the nucleus of comet 67P/Churyumov-Gerasimenko. *Astron. Astrophys.* **583**, A17 (2015). doi:10.1051/0004-6361/201526049

69. D. Prialnik, J. Benkhoff, M. Podolak, "Modeling the structure and activity of comet nuclei" in *Comets II*, M. C. Festou, H. U. Keller, H. A. Weaver Eds. (Univ. of Arizona Press, Tucson, 2004), pp. 359–387.

70. W. C. Fraser, M. E. Brown, A. Morbidelli, A. Parker, K. Batygin, The absolute magnitude distribution of Kuiper Belt Objects. *Astrophys. J.* **782**, 100 (2014). doi:10.1088/0004-637X/782/2/100

71. R. Li, A. N. Youdin, J. B. Simon, Demographics of planetesimals formed by the streaming instability. *Astrophys. J.* **885**, 69 (2019). doi:10.3847/1538-4357/ab480d

72. H. J. Melosh, *Impact Cratering: A Geologic Process* (Oxford Univ. Press, Oxford, 1989).

73. H. Sierks, C. Barbieri, P. L. Lamy, R. Rodrigo, D. Koschny, H. Rickman, H. U. Keller, J. Agarwal, M. F. A'Hearn, F. Angrilli, A.-T. Auger, M. A. Barucci, J.-L. Bertaux, I. Bertini, S. Besse, D. Bodewits, C. Capanna, G. Cremonese, V. Da Deppo, B. Davidsson, S. Debei, M. De Cecco, F. Ferri, S. Fornasier, M. Fulle, R. Gaskell, L. Giacomini, O. Groussin, P. Gutierrez-Marques, P. J. Gutiérrez, C. Güttler, N. Hoekzema, S. F. Hviid, W.-H. Ip, L. Jorda, J. Knollenberg, G. Kovacs, J. R. Kramm, E. Kührt, M. Küppers, F. La Forgia, L. M. Lara, M. Lazzarin, C. Leyrat, J. J. Lopez Moreno, S. Magrin, S. Marchi, F. Marzari, M. Massironi, H. Michalik, R. Moissl, S. Mottola, G. Naletto, N. Oklay, M. Pajola, M. Pertile, F. Preusker, L. Sabau, F. Scholten, C. Snodgrass, N. Thomas, C. Tubiana, J.-B. Vincent, K.-P. Wenzel, M. Zaccariotto, M. Pätzold, Cometary science. On the nucleus structure and activity of comet 67P/Churyumov-Gerasimenko. *Science* **347**, aaa1044 (2015). doi:10.1126/science.aaa1044 Medline

74. M. F. A'Hearn, M. J. S. Belton, W. A. Delamere, L. M. Feaga, D. Hampton, J. Kissel, K. P. Klaasen, L. A. McFadden, K. J. Meech, H. J. Melosh, P. H. Schultz, J. M. Sunshine, P. C. Thomas, J. Veverka, D. D. Wellnitz, D. K. Yeomans, S. Besse, D. Bodewits, T. J. Bowling, B. T. Carcich, S. M. Collins, T. L. Farnham, O. Groussin, B. Hermalyn, M. S. Kelley, M. S. Kelley, J.-Y. Li, D. J. Lindler, C. M. Lisse, S. A. McLaughlin, F. Merlin, S. Protopapa, J. E. Richardson, J. L. Williams, EPOXI at comet Hartley 2. *Science* **332**, 1396–1400 (2011). doi:10.1126/science.1204054 Medline

75. J. Veverka, K. Klaasen, M. A'Hearn, M. Belton, D. Brownlee, S. Chesley, B. Clark, T. Economou, R. Farquhar, S. F. Green, O. Groussin, A. Harris, J. Kissel, J.-Y. Li, K. Meech, J. Melosh, J. Richardson, P. Schultz, J. Silen, J. Sunshine, P. Thomas, S. Bhaskaran, D. Bodewits, B. Carcich, A. Cheuvront, T. Farnham, S. Sackett, D. Wellnitz, A. Wolf, Return to Comet Tempel 1: Overview of Stardust-NExT results. *Icarus* **222**, 424–435 (2013). doi:10.1016/j.icarus.2012.03.034

76. D. E. Brownlee, F. Horz, R. L. Newburn, M. Zolensky, T. C. Duxbury, S. Sandford, Z. Sekanina, P. Tsou, M. S. Hanner, B. C. Clark, S. F. Green, J. Kissel, Surface of young Jupiter family comet 81P/Wild 2: View from the Stardust Spacecraft. *Science* **304**, 1764–1769 (2004). doi:10.1126/science.1097899 Medline

77. L. A. Soderblom, T. L. Becker, G. Bennett, D. C. Boice, D. T. Britt, R. H. Brown, B. J. Buratti, C. Isbell, B. Giese, T. Hare, M. D. Hicks, E. Howington-Kraus, R. L. Kirk, M. Lee, R. M. Nelson, J. Oberst, T. C. Owen, M. D. Rayman, B. R. Sandel, S. A. Stern, N. Thomas, R. V. Yelle, Observations of comet 19P/Borrelly by the miniature integrated camera and spectrometer aboard Deep Space 1. *Science* **296**, 1087–1091 (2002). doi:10.1126/science.1069527 Medline

78. B. J. Buratti, M. D. Hicks, L. A. Soderblom, D. Britt, J. Oberst, J. K. Hillier, Deep Space 1 photometry of the nucleus of Comet 19P/Borrelly. *Icarus* **167**, 16–29 (2004). doi:10.1016/j.icarus.2003.05.002

79. J. R. Spencer *et al*., Data archive for Spencer et al. 2020, The geology and geophysics of Kuiper Belt object (486958) Arrokoth, Science, figshare (2020); https://doi.org/10.6084/m9.figshare.11485443.

80. R. A. Beyer, O. Alexandrov, S. McMichael, The Ames Stereo Pipeline: NASA's Open Source Software for Deriving and Processing Terrain Data. *Earth Space Sci.* **5**, 537–548 (2018). doi:10.1029/2018EA000409

81. R. A. Beyer, O. Alexandrov, S. McMichael, NeoGeographyToolkit/StereoPipeline: NASA Ames Stereo Pipeline 2.6.1 (Version v2.6.1). Zenodo (2018), https://doi.org/10.5281/zenodo.1345235.

82. Y. Chen, G. Medioni, Object modelling by registration of multiple range images. *Image Vis. Comput.* **10**, 145–155 (1992). doi:10.1016/0262-8856(92)90066-C

83. P. J. Besl, N. D. McKay, A method for registration of 3-D shapes. *IEEE Trans. Pattern Anal. Mach. Intell.* **14**, 239–256 (1992). doi:10.1109/34.121791

84. J. A. Skinner *et al*., Planetary Geologic Mapping Protocol-2018. US Geological Survey, Flagstaff, AZ (2018). https://planetarymapping.wr.usgs.gov/Page/view/Guidelines

85. K. N. Singer, W. B. McKinnon, L. T. Nowicki, Secondary craters from large impacts on Europa and Ganymede: Ejecta size–velocity distributions on icy worlds, and the scaling of ejected blocks. *Icarus* **226**, 865–884 (2013). doi:10.1016/j.icarus.2013.06.034

86. E. B. Bierhaus, A. S. McEwen, S. J. Robbins, K. N. Singer, L. Dones, M. R. Kirchoff, J.-P. Williams, Secondary craters and ejecta across the solar system: Populations and effects on impact-crater-based chronologies. *Meteorit. Planet. Sci.* **53**, 638–671 (2018). doi:10.1111/maps.13057

87. J. M. Moore, W. B. McKinnon, D. P. Cruikshank, G. R. Gladstone, J. R. Spencer, S. A. Stern, H. A. Weaver, K. N. Singer, M. R. Showalter, W. M. Grundy, R. A. Beyer, O. L. White, R. P. Binzel, M. W. Buie, B. J. Buratti, A. F. Cheng, C. Howett, C. B. Olkin, A. H. Parker, S. B. Porter, P. M. Schenk, H. B. Throop, A. J. Verbiscer, L. A. Young, S. D. Benecchi, V. J. Bray, C. L. Chavez, R. D. Dhingra, A. D. Howard, T. R. Lauer, C. M. Lisse, S. J. Robbins, K. D. Runyon, O. M. Umurhan, Great expectations: Plans and predictions for New Horizons encounter with Kuiper Belt Object 2014 MU69 ("Ultima Thule"). *Geophys. Res. Lett.* **45**, 8111–8120 (2018). doi:10.1029/2018GL078996

88. J.-Y. Li, S. Besse, M. F. A'Hearn, M. J. S. Belton, D. Bodewits, T. L. Farnham, K. P. Klaasen, C. M. Lisse, K. J. Meech, J. M. Sunshine, P. C. Thomas, Photometric properties of the nucleus of Comet 103P/Hartley 2. *Icarus* **222**, 559–570 (2013). doi:10.1016/j.icarus.2012.11.001

89. S. Fornasier, P. H. Hasselmann, M. A. Barucci, C. Feller, S. Besse, C. Leyrat, L. Lara, P. J. Gutierrez, N. Oklay, C. Tubiana, F. Scholten, H. Sierks, C. Barbieri, P. L. Lamy, R. Rodrigo, D. Koschny, H. Rickman, H. U. Keller, J. Agarwal, M. F. A'Hearn, J.-L. Bertaux, I. Bertini, G. Cremonese, V. Da Deppo, B. Davidsson, S. Debei, M. De Cecco, M. Fulle, O. Groussin, C. Güttler, S. F. Hviid, W. Ip, L. Jorda, J. Knollenberg, G. Kovacs, R. Kramm, E. Kührt, M. Küppers, F. La Forgia, M. Lazzarin, J. J. Lopez Moreno, F. Marzari, K.-D. Matz, H. Michalik, F. Moreno, S. Mottola, G. Naletto, M. Pajola, A. Pommerol, F. Preusker, X. Shi, C. Snodgrass, N. Thomas, J.-B. Vincent, Spectrophotometric properties of the nucleus of comet 67P/Churyumov-Gerasimenko from the OSIRIS instrument onboard the ROSETTA spacecraft. *Astron. Astrophys.* **583**, A30 (2015). doi:10.1051/0004-6361/201525901

90. P. L. Lamy, I. Toth, Y. R. Fernandez, H. A. Weaver, "The sizes, shapes, albedos, and colors of cometary nuclei". In *Comets II*, M. C. Festou, H. U. Keller, H. A. Weaver Eds. (University of Arizona Press, Tucson 2004) 223-264.